

Numerical and Experimental Characterization of High Enthalpy Flow in an Expansion Tunnel Facility

Matthew MacLean¹Aaron Dufrene²Timothy Wadhams³Michael Holden⁴*CUBRC / LENS, Buffalo, NY 14225*

Several tools have been developed to perform rapid simulations of the relevant physics of an expansion tunnel facility in preparation for the operation of the LENS-XX tunnel. These tools have been assembled to provide multiple mechanisms to analyze the performance of the facility. Two algorithms have been employed in this effort to provide nearly instantaneous computations of the freestream state of the test gas – a characteristics based code and a quasi one-dimensional, unsteady code. These two codes have been modified to include thermal and chemical excitation that has been shown to be essential for this type of simulation. In addition, full unsteady Navier-Stokes simulations have been performed to study viscous effects in the facility and two-dimensional behavior to contrast the simplified algorithms. These codes are currently undergoing validation with available data from the facility to anchor the numerical codes and to assess and understand the experimental data.

Nomenclature

a	speed of sound	W	shock velocity
b_k^0	initial elemental composition	\dot{w}	chemical source term
b_{0M}	non-ideal gas correction	X	species concentration or position
e	energy	α	stoichiometric coefficient
h	enthalpy	η	mole-mass ratio
m	cell mass	Λ	Lagrange multiplier
M	molecular weight	μ_j^0	specific Gibbs free-energy
P	pressure	ρ	density
R	universal gas constant	τ	vibrational relaxation constant
\tilde{R}	mixture gas constant	<u>subscripts</u>	
s	entropy	D	downstream of shock
T	temperature	P	primary system
t	time	S	secondary system
U	velocity	U	upstream of shock
V	cell volume		

I. Introduction

ACCURATE duplication of the flight of vehicles at hypersonic speeds for research, propulsion, cruise, strike, or reentry applications requires well-characterized ground test facilities to mitigate the risk of expensive flight tests and the danger to scientific payloads or human passengers. CUBRC has spent the past decade working to validate the operation of the LENS reflected shock tunnel facilities through detailed comparisons with state-of-the-art numerical predictions for a range of test article shapes and relevant physical phenomena. Through this process,

¹ Senior Research Scientist; Senior Member AIAA; maclean@cubrc.org.

² Research Scientist; Member AIAA; dufrene@cubrc.org.

³ Research Scientist; Senior Member AIAA; wadhams@cubrc.org.

⁴ Vice President of Hypersonics; Fellow AIAA; holden@cubrc.org.

both the experimental facilities and the CFD codes/algorithms have been simultaneously validated and the capabilities to design vehicles using experimental and computational methods have been advanced significantly.

At the same time, we have recognized the need to more accurately duplicate the environment of very high velocity flight. The need to better understand the physical processes that dominate hypersonic environments requires innovation in the area of ground test facilities and their capabilities. Although reflected shock tunnels offer capabilities to study the performance of vehicles with large Reynolds numbers under duplicated velocity conditions, the chemical and thermodynamic excitation that occurs in the reservoir and which remains frozen in the freestream at velocities of 4 km/s and above (particularly at very low unit Reynolds numbers) makes understanding the measured data significantly more difficult. In response to this need, we have designed and built a large-scale expansion tunnel facility LENS-XX where the freestream test gas is never stagnated prior to flowing over the model. Because kinetic energy is added directly to the gas, the freestream flow is thermochemically quiescent as it is in free-flight. This facility allows us to better duplicate the physics of higher energy flows from 10 MJ/kg up to 100 MJ/kg for reentry applications and complements the capabilities of the reflected shock tunnels which best targets conditions at 10 MJ/kg and lower.

In this work, we begin the process of validation for this new type of facility, beginning with determining freestream conditions, test times, and basic flowfield comparisons just as has been done with the reflected shock tunnels. This process has utilized lessons learned from the reflected shock tunnel experience to describe the thermochemical modeling of the gas in the most efficient manner. The computation of the conditions in the expansion tunnel facility has been analyzed with emphasis on developing and validating tools that offer the best balance between accuracy and speed such that the rapid analysis of the experimental measurements we have provided in the past is maintained in this facility. The results of this process will be an expansion tunnel facility that has undergone the necessary scrutiny and validation to become the world's first large-scale, production expansion tunnel facility to study the problem of planetary reentry.

II. Experimental Facility Background

Currently, CUBRC operates the 48" reflected shock tunnel, the LENS-I and LENS-II reflected shock tunnels¹, and the LENS-XX expansion tunnel². The reflected shock tunnel uses shocks to heat and pressurize a stagnant test gas to high enthalpy levels. This test gas may then be expanded through a converging-diverging nozzle in a manner similar to a blowdown facility to produce a hypervelocity test flow. Expansion tunnels like LENS-XX also operate as short duration facilities, but an expansion tunnel produces a high enthalpy flow without the need to first stagnate the test gas. In an expansion tunnel, the bulk of the test gas energy is added through an unsteady expansion

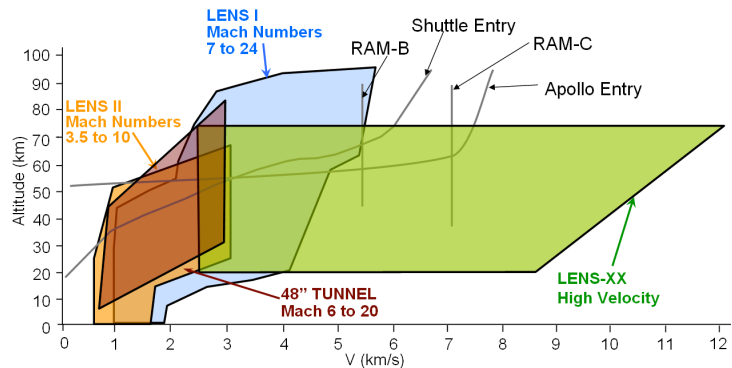


Figure 1. Nominal Capability Map of CUBRC Facilities to Duplicate Freestream Conditions in Air

in the acceleration segment of the tunnel to produce a low static temperature, high velocity test gas which is then isentropically expanded in a diverging nozzle to achieve a high enthalpy test flow at a thermodynamic state like that of a flight condition. The result is a freestream flow that is free of frozen, dissociated chemical contamination that can occur reflected shock facilities at enthalpies exceeding 10 MJ/kg. While the useable test times from an expansion tunnel are generally shorter than those from a reflected shock tunnel, the clean, very high enthalpy flows that an expansion tunnel can generate provides a unique testing capability. A notional range of velocity and altitude duplication capabilities for all the LENS facilities is given using air test gas in Fig. 1.

The LENS reflected shock-tunnel facilities were developed primarily to study the full-scale, hypervelocity flow physics of interceptors and air-breathing engine configurations. The scale and flow duplication capabilities of LENS are such that these vehicles can be studied at their full scale, inclusive of effects such as transition to turbulence, turbulent mixing from cross-flow jets and thrusters, duplicated flow chemistry and other effects that are difficult or impossible to simulate at cold-flow or sub-scale conditions. Besides aerothermal measurements, extensive studies in this facility have been made using non-intrusive diagnostics such as aero-optic and aero-acoustic measurements, including recent work with tunable laser-diode diagnostics³. The capabilities of LENS-I duplicate the flight conditions of interceptors and scramjet engines from Mach 7 to 15 (with Reynolds number matching to

Mach 22), while the LENS-II facility complements it in such a way that this capability is seamlessly extended down to Mach 3.5 at sea level density. The LENS-XX expansion tunnel facility duplicates the flight conditions of very high-speed vehicles traveling from Mach 10 to 30+.

III. Overview of Expansion Tunnel

The expansion tunnel works very differently than a reflected shock tunnel facility. Reflected shock tunnels operate by driving strong incident and reflected shocks through the test gas which results in a high pressure, high temperature, stagnant reservoir which can be expanded through a converging-diverging nozzle like a blowdown facility. Expansion tunnels do not stagnate the test gas at any time before it flows over the test article. Instead, the test gas is set into motion by a single shock of only weak to moderate strength, and the bulk of the energy in the flow is added to kinetic energy directly by using an unsteady acceleration to increase the velocity. A wave diagram of the basic states of the expansion tunnel is given in Fig 2. In this figure, position is plotted schematically along the horizontal axis and time is plotted qualitatively along the vertical axis. The three test chambers are filled to different pressures and initially separated by diaphragms, where the primary diaphragm between the driver and test gas sections is broken at a time designated as zero. The waves in the diagram are shocks (red), contact surfaces (dotted green) or isentropic expansion fans (blue), where the thermodynamic state and/or composition of the gases change across any of the waves. Important thermodynamic states of the gases are numbered and the label is colored by the gas composition.

The driver gas (state 4) is a very high pressure, heated, low molecular weight gas (typically hydrogen or helium) that causes a primary shock of moderate strength to move through the test gas when the primary diaphragm is broken. This shock raises the pressure in the test gas just sufficiently to break the secondary diaphragm and causes an initial velocity toward the right in the schematic (state 2). The peak temperature of the test gas during the entire excitation process occurs at state 2, which is typically on the order of 2,000 – 3,000 K or approximately an order of magnitude lower than a comparable freestream condition in a reflected shock tunnel. The moving test gas then accelerates into a much lower pressure acceleration segment that is typically at nearly vacuum (state 10). This causes the test gas to cool and accelerate to very high velocities, given by state 5.

This is the freestream state of the test gas at the end of the tube. The freestream velocity obtained is primarily dependent on the molecular weight of the driver gas, the pressure of the driver gas, and the vacuum level of the acceleration segment. Test time available for testing begins at the contact surface between states 20 and 5 and lasts until either the tail of the left-running expansion between states 2 and 5 reaches the test station or until the reflected head of the same wave reaches the test station⁵.

The freestream state of the gas typically has a translational temperature near 300K with a very high velocity. The relative strengths of the primary shock (state 1 to state 2) and the unsteady expansion (state 2 to state 5) can be utilized to generate different Mach numbers and test conditions for a given total pressure ratio (P_4/P_{10}) which provides a significant degree of flexibility for the facility.

IV. Determination of Freestream State with a Characteristics Based Approach

As a first mechanism to determine the freestream state of the test gas, a characteristics based solution algorithm has been created to compute the flow properties based on measured and inferred parameters. This code follows closely the algorithm developed by Miller⁸ for the original Langley expansion tube⁹, and has been named the *CUBRC High Enthalpy Expansion Tunnel Analysis (CHEETAh)* code. The goal of the development of this code was to create a numerical tool that is robust and provides instant freestream state definitions but still retains enough of the physics of the expansion tunnel process to be meaningful. The states labeled in Fig 2 are computed as functions of a primary wave system consisting of states 1, 2, 3, and 4 and a secondary wave system consisting of

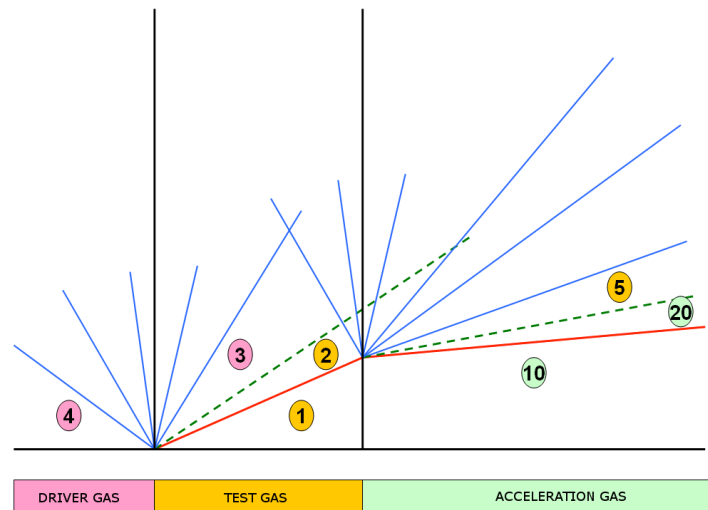


Figure 2. X-t Wave Diagram of an Expansion Tunnel

states 2, 10, 20, and 5 by exactly computing the real jump conditions across each wave. The system is solved iteratively including the possibilities for frozen or equilibrium chemistry and frozen or equilibrium thermodynamic behavior in each state zone. In the case of the primary system, the code allows for either a measured driver pressure (P_d) or a measured primary shock speed (W_p) to be specified, but not both. In the case of the secondary system, the code allows for either the acceleration tube pressure (P_{10}) or a secondary shock speed (W_s) to be specified, but not both.

Both the primary wave system and the secondary wave system are defined by the jump conditions across a normal shock for mass, momentum, and energy, given by Eqns (1-3), the integration relationship across an upstream facing unsteady expansion wave given in Eqn (4), and an equation of state (discussed further below). The case where the primary shock speed is known is the simplest case because the post-shock State 2 is completely known from initial conditions and W_p . The effective driver pressure may be computed by integrating Eqn (4) in reverse back to zero velocity for isentropic flow. For cases where the shock speed is known or the downstream pressure or the secondary system is unknown, the system is fully coupled and must be solved iteratively. However, perfect gas relations may be used to compute reasonable initial guesses for a robust numerical solver.

$$\rho_U W = \rho_D (W - U_D) \quad (1)$$

$$\rho_U W^2 + P_U = \rho_D (W - U_D)^2 + P_D \quad (2)$$

$$h_U + \frac{1}{2} W^2 = h_D + \frac{1}{2} (W - U_D)^2 \quad (3)$$

$$\int dU = - \int \left(\frac{dh}{a} \right)_s \quad (4)$$

The code employs a “black-box” routine to compute the equilibrium composition of an arbitrary set of species for any state given any two thermodynamic variables, where the most common pairings are (P, T), (P, ρ), (T, ρ), (P, s), or (P, h). Gibbs or Helmholtz free energy is minimized as outlined below. Additionally, individual species thermodynamic energies are computed assuming fully excited translational and rotational modes (with one exception detailed below), a simple-harmonic oscillator vibrational model for diatomic and triatomic species, and electronic energy modes collected from a database of published sources. This routine forms the equation of state when equilibrium chemistry is selected as a model.

A. Computation of Equilibrium Chemistry Composition

The computation of the equilibrium composition of any gas mixture as a function of two thermodynamic state variables is performed using the free-energy minimization technique of Gordon and McBride¹⁰. This is the same technique that is utilized in the CEA code. Their technique casts the composition of the system in terms of mole-mass ratio and employs the natural log of all variables in the system, which ensures very robust convergence.

The Gibbs system for specified (P, T) consists of a Gibbs energy equation for each species, given in Eqn (5),

$$\left(\frac{\mu_j^0}{RT} \right) + \ln \left(\frac{\eta_j}{\eta} \right) + \ln \left(\frac{P}{P_{REF}} \right) + \sum_{k=1}^{NE} \alpha_{kj} \Lambda_k = 0 \quad (5)$$

a total mass equation, given in Eqn (6),

$$\sum_{j=1}^{NS} \eta_j - \eta = 0 \quad (6)$$

and one or more elemental conservation constraints enforced using LaGrange multipliers given in Eqn (7).

$$\sum_{j=1}^{NS} \alpha_{kj} \eta_j - b_k^0 = 0 \quad (7)$$

The system given in Eqns (5), (6), and (7) is iterated to convergence using Newton iteration for the variable set $[\ln(\eta_{1-NS}), \ln(\eta), \Lambda_{1-NE}]$. An additional variable, $\ln(T)$, is added for systems where the temperature is not a specified constant. The system is quite robust and converges rapidly, usually in 20 – 30 iterations. Convergence is slower at low temperatures and pressures, but application of numerical limiting as described by Gordon and McBride has produced robust convergence at all conditions and chemical systems studied.

Data to compute the Gibbs energy at standard state is also obtained from the extensive set of tables provided by McBride, et al¹⁹. The tabulated data are smoothly varying functions of temperature, typically in the range of 200 – 20,000 K. A constant specific heat is assumed outside this range to preserve solver continuity and avoid any convergence errors or erratic behavior during the early iterations.

Finally, with a converged system, secondary parameters such as equilibrium sound speed, specific heat ratio, derivatives with respect to temperature, pressure, and other thermodynamic variables can be obtained by differentiating Eqns (5), (6), and (7) and solving the system one final time. The equilibrium sound speed is utilized within the unsteady expansion relation in Eqn (4) for the primary and secondary systems to compute the properties through the expansion waves.

B. Modeling of Rotational Excitation of Hydrogen Gas

The LENS-XX facility is somewhat unique among the few expansion tunnels in the world because it employs warm hydrogen as a primary driver gas. Other facilities use an arc heater¹¹, a combustor driver⁷, a piston driver¹², or are restricted to low to moderate energy flows with a helium driver⁵. Hydrogen offers several advantages. It acts as an ideal piston without the inertial tailoring or heating issues associated with physical pistons. Also, because the driver gas cools from its initial state, there is no extraneous radiation emitted which might influence spectroscopy or other sensitive non-intrusive diagnostic measurements. However, it was discovered during the development of this code that there is an effect unique to hydrogen, which must be considered in modeling the dynamics of the flow.

The hydrogen driver, which is typically heated by only a few hundred degrees above room temperature prior to firing, cools dramatically through the expansion process in the primary system. At very large pressure ratios designed to produce very high-energy test flows, this expansion can be quite strong and cools the hydrogen gas nearly to its condensation point around 20K. Although, most often, cold diatomic gases are considered to be ideal with fully excited translational and rotational modes (resulting in a constant specific heat ratio of 1.40), hydrogen is special in that its characteristic rotational temperature is very high, about 85K. Therefore, through most of the expansion process occurring in the facility, the rotational energy component of hydrogen cannot be considered to be fully excited.

The situation was found to be even more complex because the nuclei of diatomic hydrogen are fermions, which must be described by antisymmetric, total wave functions¹⁷. Molecules with even, symmetric rotation states must have odd, antiparallel spin states to meet this requirement and are referred to as para-hydrogen molecules (a singlet state). Molecules with odd, asymmetric rotational states must have even, parallel spin states and are referred to as ortho-hydrogen molecules (a triplet state). These two types of hydrogen molecules are so fundamentally different that they may be thought of as a mixture of two different gases. Because the state transition from one type to the other must occur with simultaneous rotational and spin transitions (a very low probability in the absence of a third body), pure hydrogen gas is very slow to rotationally equilibrate to a new temperature when the gas is heated or cooled. At room temperature and above, the ratio of ortho- to para- is approximately 3:1 (a reflection of the degeneracy of the two states), but at

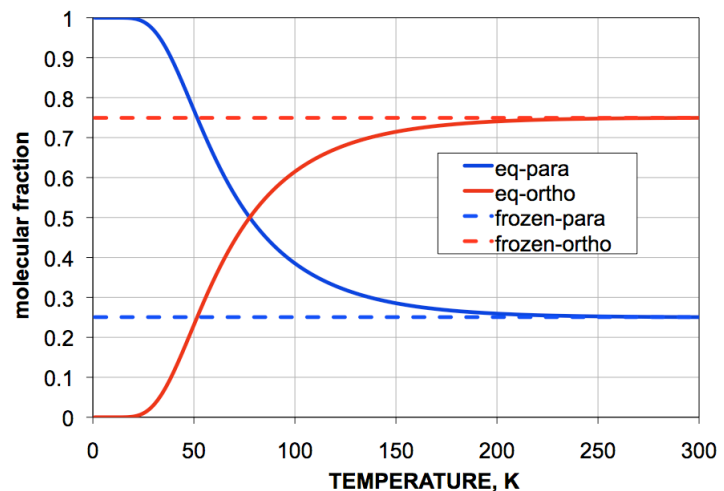


Figure 3. Rotational Specific Heat of Diatomic Hydrogen at Low Temperatures

temperatures close to 0 K, the equilibrium state is dominated almost exclusively by the para- form as shown in Fig 3. A summary of the rotational specific heat of diatomic hydrogen is plotted in Fig 4 for various scenarios over the temperature range of interest. Four scenarios are shown: (1) the ideal value for a diatomic gas (rotation fully-excited), (2) the trend for a generic diatomic gas with the finite characteristic rotational temperature of 85K, (3) the trend assuming an equilibrium distribution of ortho- and para- states at the given temperature, and (4) a trend assuming that the ratio of ortho- and para- forms is frozen at the room temperature composition. Since the expansion process occurs over a millisecond time-scale, the frozen approximation seems to be the most realistic for this situation.

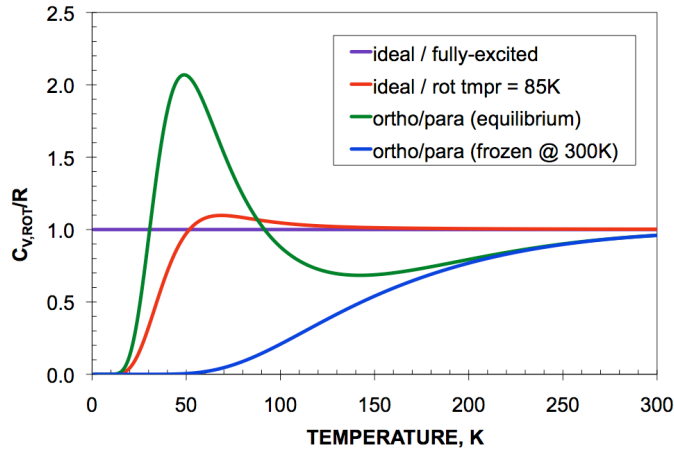


Figure 4. Rotational Specific Heat of Diatomic Hydrogen at Low Temperatures

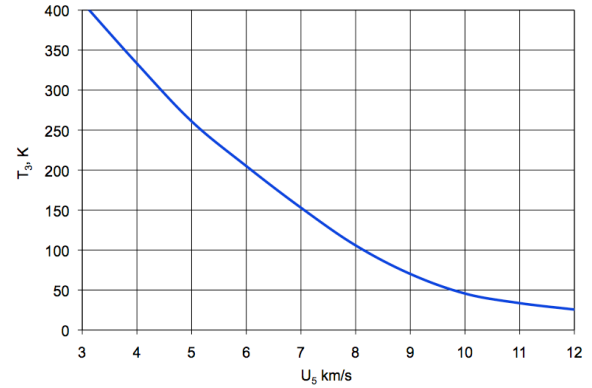


Figure 5. Typical Post-Expansion Hydrogen Temperature (T_3) for Range of Test Condition Velocity (U_5)

The modeling of hydrogen at these cold temperatures is significant because the integration of the isentropic expansion process through the temperature range is a function of the shape of the curve of specific heat. This is evident by reviewing Eqn (4) for the unsteady expansion of the hydrogen driver gas and noting that dh in the integral is directly related to C_p . The equilibrium speed of sound is also a ratio of specific heats of the gas as it is cooling.

The amount of expansion required to produce a test condition of a given enthalpy (velocity) level can vary somewhat depending on the relative strength of the primary shock versus the secondary test gas expansion, but a nominal set of computations has been performed for a series of velocity increments to show the temperature that the hydrogen cools off to through the expansion in Fig 5. As can be observed, at even moderate enthalpy conditions, the hydrogen has cooled to the point at which the approximation of a fully-excited rotational diatomic can no longer be justified, and at extreme conditions, the temperature is severe and near the condensation point.

C. Modeling of Non-ideal Gas Behavior at High Pressure

Large densities are often present in the driver gas because of the high pressure and relatively low temperatures, so the ideal gas law does not strictly apply. Instead, we have used the excluded volume correction of Lordi and Mates¹⁵ to account for these dense states. In the excluded volume approach, the ideal gas law is modified to exclude the volume occupied by the gas molecules at high density. This relation is given in Eqn (8).

$$P = \frac{\rho \tilde{R} T}{(1 - b_{0M} \rho)} \quad (8)$$

Here, the constant b_{0M} , called the co-volume, is a term involving the effective molecular diameter of the gas. One can see that for small to moderate densities, the ideal gas law is approximately returned, while the excluded volume effect becomes significant only for large densities. The enthalpy, entropy, and speed of sound of the gas are also modified accordingly by the excluded volume equation. This same approach has also been implemented by Candler¹⁴ to account for the similarly high densities present in the reservoir region of the reflected shock tunnels, and the correction seems to bring the predictions more in line with measured Pitot profiles and static pressure measurements in the freestream.

Effective Molecular diameters for all the gases employed in the expansion tunnel are obtained from the tabulated data by Svehla¹⁶. This effect is only significant for the undisturbed driver state 4, which is almost always hydrogen or helium. However, for driver pressures at or near 70 MPa (10,000 psia), the effect of the non-ideal gas correction to the equation of state can be considerable. A series of solutions was computed with the code by specifying values of driver pressure and computing the primary and secondary shock speeds. The results with and without the non-ideal equation of state is shown in Fig 6. Increasing the driver pressure increases, among other things, the unit Reynolds number of the freestream state 5. However, as Fig 6 shows, the unit Reynolds number obtained is dramatically under-predicted if the non-ideal gas correction is neglected.

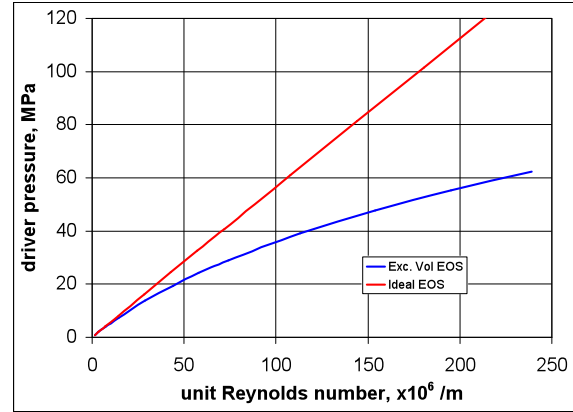
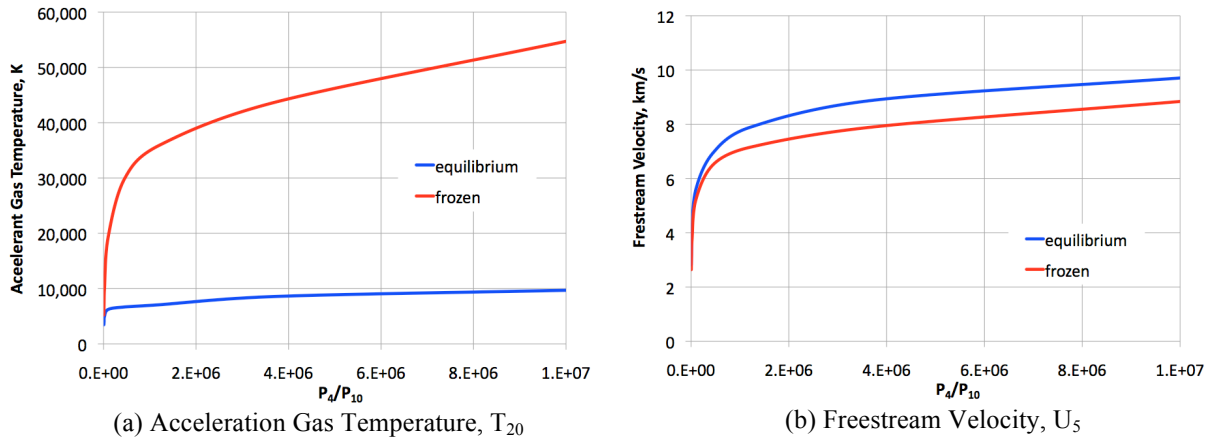


Figure 6. Effect of Non-ideal Equation of State on Freestream Velocity

D. Comparison of Calorically Perfect to Mixtures in Thermal and Chemical Equilibrium

Finally, the comparison of a series of cases for simulations assuming calorically perfect gas behavior (frozen gas composition and neglecting vibrational and electronic excitation) to cases with full chemical and thermal



(a) Acceleration Gas Temperature, T_{20}
 (b) Freestream Velocity, U_5
Figure 7. Comparison of Frozen and Equilibrium Gas Assumptions on Post Secondary Shock Accelerant Temperature and Freestream Velocity

equilibrium is considered. The most apparent differences occur in the gases downstream of the primary and incident shock where chemical dissociation and thermodynamic excitation absorb significant amounts of energy and result in much lower temperatures than the perfect gas predictions. This is shown in Fig 7(a), which plots the post secondary shock temperature T_{20} for a range of total (driver to acceleration) pressure ratios.

The differences between assuming frozen or equilibrium excitation also can have a significant effect on the unsteady (isentropic) expansion process at enthalpy levels high enough that vibrational or chemical reactivity of the expanding gas occurs. This effect is shown in Fig 7(b), which plots the differences in freestream velocity for a range of total facility pressure ratios. At the extreme

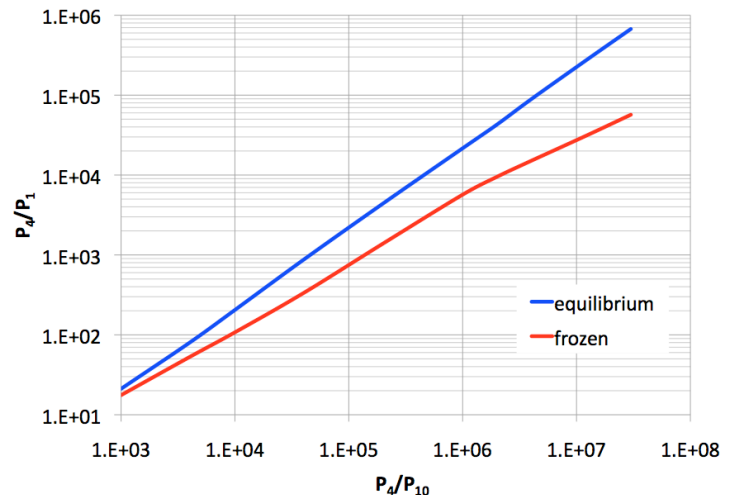


Figure 8. Comparison of Pressure Ratio Required for Maximum Test Time for Frozen and Equilibrium Gases

maximum, the difference between frozen and equilibrium assumptions results in more than 1 km/s difference in predicted freestream velocity.

The difference between frozen and equilibrium gases is also apparent in determining the ratio of pressures required in the three sections of the facility that are required to maximize the test time. This is plotted in Fig 8, which plots the total facility pressure ratio P_4/P_{10} against the driver to test gas pressure ratio P_4/P_1 . The functional dependence between these quantities is a quantitative metric of the amount of energy addition by shock heating compared to the amount of energy addition by unsteady expansion. At high enthalpy levels, the P_4/P_1 ratio (shown on a log scale) differs by as much as an order of magnitude. One way to assess the validity of these models will be to make measurements of the test time for different combinations of P_4/P_{10} and P_4/P_1 in the LENS-XX facility to quantitatively determine which of these models is closest to observed operation for different conditions.

V. Simulation of Unsteady Operation of Facility in One Dimension

A characteristics based solution based on measured inputs provides a mechanism to make an accurate estimate to the freestream conditions that is anchored to each experiment. The capability to perform calculations with frozen and equilibrium chemistry and thermodynamic contributions provides a mechanism to bound the freestream state and to determine the importance of those physical contributions. However, a method to assess the impact of finite rate chemistry and thermodynamic relaxation is needed which cannot be integrated into the *CHEETAH* solution.

A second code for the expansion tunnel facility called *Jaguar* has been developed to perform one-dimensional and quasi one-dimensional simulations of shocktube and expansion tunnel facilities. This code is based on the algorithm employed in the *LID* code of Jacobs¹³ but has been extended to include finite rate chemistry and thermodynamics.

The *LID* algorithm is a one-dimensional Lagrangian CFD code. For shocktube applications, this framework greatly simplifies the evaluation of the fluxes at the cell interfaces since the grid convects with the flow. It has also been found that this framework is beneficial on a practical level since it is not necessary to cluster grid points around discontinuities (that move with time in these types of problems). Since grid points move with the flow velocity, grid cells tend to naturally cluster so that a uniform initial grid can be simply generated for any problem. The flux is evaluated using the approximate Riemann solver developed by Jacobs¹⁸ and used for the *LID* code. A modification has been made to this flux scheme to account for variable values of specific heat ratio by solving using Jacobs' formulation and then performing several relaxation sweeps to determine the non-linear component. However, in the test cases run so far, the non-linear extension seems to make little difference and the results obtained are generally consistent with Jacobs' method. As with *LID*, the code is explicit and is second order accurate in both time and space. A source term accounts for changing area that can either be physical (inviscid) or can be utilized as a mechanism to account for approximate viscous effects. The code is not as fast as the *CHEETAH* code, but does run on the order of a minute depending on the number of time steps selected and the problem scale.

The chemical and vibrational source terms are treated as a series of reactions occurring within the current volume of each static cell since total mass is conserved within each individual cell and must be preserved. The rate of vibrational or chemical reaction increases or decreases proportionally to the density in each cell, which varies inversely with the changing cell volume. The rate of chemical production of each species is given in the usual way in Eqn (9). This is the same expression that is used in finite volume CFD formulations. From this, the rate of both chemical and vibrational relaxation may be computed from Eqns (10) and (11).

$$\dot{w}_k = M_k \sum_{r=1}^{NR} (v_{krf} - v_{krb}) \left[-k_{fr} \prod_{i=1}^{NS} X_i^{v_{irf}} + k_{br} \prod_{i=1}^{NS} X_i^{v_{irb}} \right] \quad (9)$$

$$\left. \frac{\partial(m_k)}{\partial t} \right|_j = V_j M_k \dot{w}_k \quad (10)$$

$$\left. \frac{\partial(e_v)}{\partial t} \right|_j = \sum_m \frac{e_{v,m}^* - e_{v,m}}{\tau_m} + \sum_k e_{v,k} \frac{M_k \dot{w}_k}{\rho_k} \quad (11)$$

The time-dependent results can be visualized using position on the X-axis and time on the Y-axis to produce a numerically generated version of the wave diagram. A sample case with a notional expansion tunnel has been run and the numerically computed wave diagram is shown in Fig 9(a), which plots contours of density. This diagram can be compared with the analytical wave diagram in Fig 2, where the shock and contact waves are evident from the tight clustering of density contours and the expansion waves from the evenly spaced fan of contour lines. Major features are noted on the diagram. The grid for an expansion tunnel case is shown in Fig 9(b). The grid, which initially consists of uniformly spaced cells, naturally convects with the flow in each station, and clusters as the volume of individual cells of fixed mass changes in response to changes in flow density.

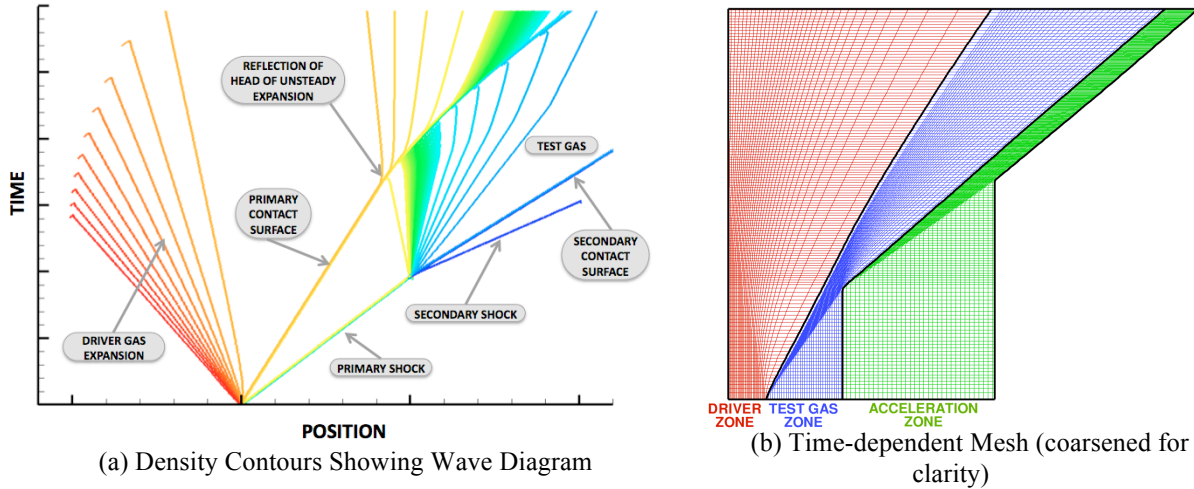


Figure 9. Numerical Wave Diagram of Density Contours and Sample Time-Dependent Mesh in Expansion Tunnel Facility

Demonstrating the chemistry and thermodynamic modeling of the tool is difficult using an expansion tunnel test case because the expansion tunnel is designed to minimize these excitations in the gas. Therefore, chemical dissociation and thermodynamic excitation is minimal in the test gas and is typically confined to only a narrow region in the accelerant gas immediately downstream of the secondary shock. A reflected shock tunnel case is a better example. A typical condition for a nominally tailored condition using a hydrogen driver and a driven test gas of air is shown in Fig 10, where temperature contours are plotted assuming perfect gas in Fig 10(a), assuming no chemical dissociation but allowing for vibrational excitation of N_2 and O_2 in Fig 10(b), and assuming chemical reactivity but no vibrational modes in Fig 10(c). The perfect gas case without chemical or thermodynamic relaxation predicts temperatures that are significantly higher than the reacting cases. The nominal reservoir temperatures are 13,000K in the perfect gas case, 10,000K for the vibrational case, and 7,000K for the chemistry case. Including both chemistry and vibration (not shown) results in even lower reservoir temperature levels. The reflected shock tunnel is also a stressful case to run because of the very high density in the reservoir region that forces the gas rapidly to chemical and vibrational equilibrium. For this condition, the equilibrium composition limiting performed inside the code is necessary for problem stability.

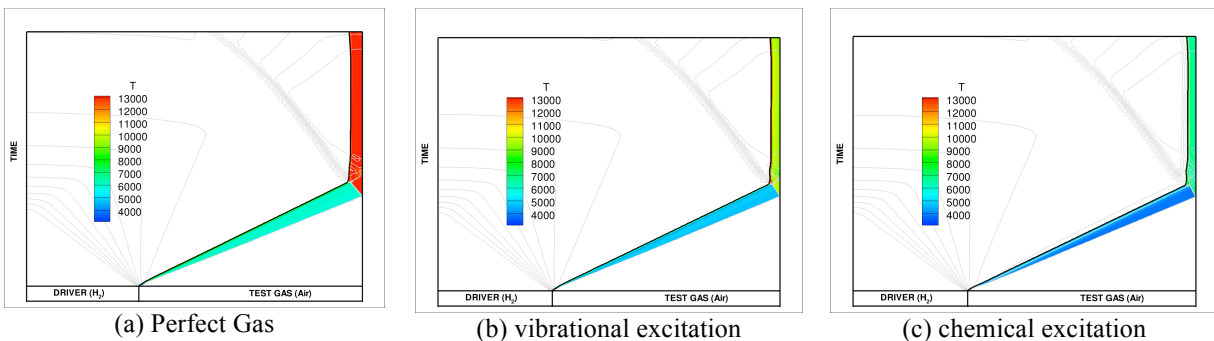


Figure 10. Reflected Shock Tunnel Case Demonstrating Use of Chemical and Thermodynamic Relaxation. Contour Coloring is of Temperature (identical scale all graphs) and Gray Contour Lines are of Pressure to Highlight Waves

VI. Full Unsteady Navier-Stokes Simulations of Expansion Tunnel Facility

The primary, production CFD tool used at CUBRC for facility design, design-of-experiment, and data validation is the DPLR code licensed by NASA Ames Research Center (ARC). DPLR is a multi-block, structured, finite-volume code that solves the reacting Navier-Stokes equations including finite rate chemistry and finite rate vibrational non-equilibrium effects. This code is based on the data-parallel line relaxation method²⁰ and implements a modified (low dissipation) Steger-Warming flux splitting approach²¹ for the convection terms and central differencing for the diffusion terms. Finite rate vibrational relaxation is modeled via a simple harmonic oscillator vibrational degree of freedom²² using the Landau-Teller model²³. Vibrational energy relaxation rates are computed by default from the semi-empirical expression due to Millikan and White²⁴, but rates from the work of Camac²⁵ and Park, et al²⁶ are substituted for specific collisions where experimental data exists. Vibration-dissociation coupling is currently modeled using the $T-T_v$ approach of Park²⁷ or with some preliminary implementation of CVDV coupling²⁸. Transport properties are appropriately modeled in DPLR for high enthalpy flow^{29,30} using the binary collision-integral based mixing rules from Gupta, et al³¹. Diffusion coefficients are modeled using the self-consistent effective binary diffusion (SCEBD) method³². Turbulence models available in the DPLR code currently include the Baldwin-Lomax 0-equation model³³, the Spalart-Allmaras model 1-equation model³⁴, and the Shear Stress Transport (SST) 2-equation model³⁵ each with corrections for compressibility effects^{36,37}.

The major feature of DPLR that is relevant to simulations of the expansion tunnel facility has been the development of a second-order accurate, dual time-stepping algorithm³⁸ in the most recent version released by NASA ARC. The dual-time mode of DPLR has enabled better temporal accuracy, significantly better stability for this type of problem, time integration steps that allow the solution to be resolved with a feasible computational expenditure, and tracking of point quantities with time. For several exploratory cases, the expansion tunnel has been simulated as an axisymmetric, constant-area tube with the driver, driven, and acceleration sections initialized to their starting gas compositions and conditions. Initially, the secondary diaphragm between the driven and acceleration segments was simulated with an inviscid wall boundary condition on both blocks. The value of pressure against this inviscid wall was tracked at each iteration and the simulation was stopped to remove the wall boundary condition when that pressure increased above the initial value. This method approximated the breaking of the secondary diaphragm during a tunnel event. The results of two cases are considered more fully in the next §VII of this paper, but a typical flow image showing contours of temperature at three critical points in time in the simulation are shown in Fig 11. In these images, the approximate zone of test gas is highlighted to more easily interpret the contours. In Fig 11(b) the shock-heated test gas has arrived at the secondary diaphragm (inviscid wall) which was subsequently turned into a zonal interface boundary condition. In Fig 11(c), the zone of very high temperature to the right of the test gas is the shock-heated accelerant gas, while the test gas is much cooler and shown in green. The driver gas is blue because it tools from its initial state.

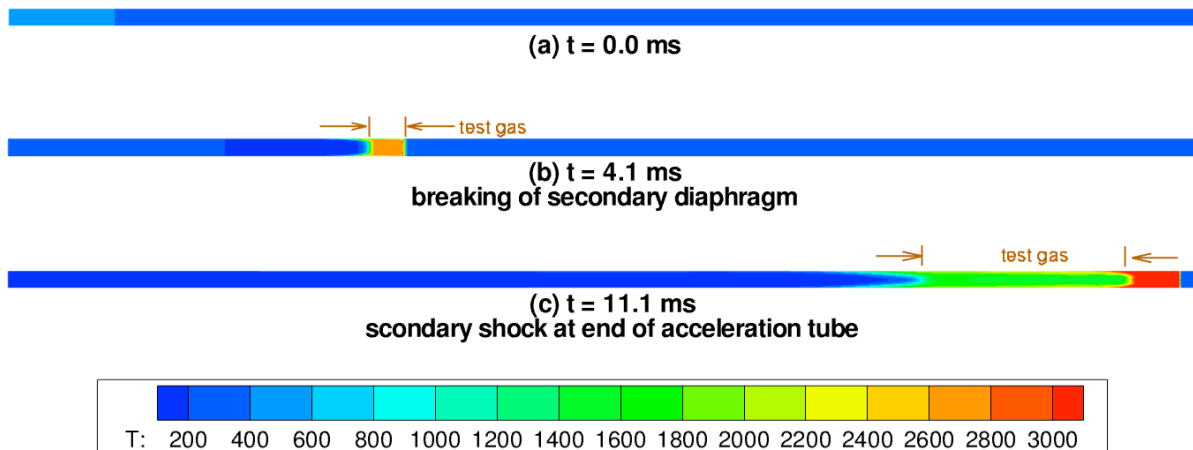


Figure 11. Temperature Contours of DPLR Unsteady Simulation at Initial State, Breaking of Secondary Diaphragm, and Arrival of Secondary Shock at the End of the Acceleration Tube

While the full Navier-Stokes simulations employed in this section have the most detailed physical and geometric models incorporated into the simulations, there are several issues that required notice. First, of course, this type of simulation is computationally expensive. Where the *CHEETAh* and *Jaguar* algorithms compute the solution in the

timeframe of a few seconds, these DPLR simulations take several days each to compute. Therefore, it is not possible to keep pace with the experimental facility, which can operate one to two times per day. Storage could also be an issue eventually since the unsteady solution data is on the order of 10GB each. Also, the solution is not particularly efficient since all cells of all blocks must be solved at each iteration. For the first part of the simulation before the secondary diaphragm is de-activated, the entire acceleration tube must be solved even though there is no gas motion at all.

There are several issues with respect to physical modeling too. Although the DPLR simulations are the only simulation technique that is able to directly incorporate turbulent boundary layer effects along the walls into the simulations, the simulations must rely on RANS models for this effect. Nompelis, et al.⁶ demonstrated that for a facility the size of LENS-XX, the boundary layer becomes fully turbulent almost immediately along the walls of the facility. The Menter SST model³⁵ was used for all the simulations performed, but the expectations of this model to simulate the inherently unsteady viscous process are low. Since the turbulence model heavily impacts the predicted uniformity of the shock, contact, and expansion wave propagation, we expect this limitation to be a primary uncertainty in the result. It is also not possible to perform any kind of rational grid clustering to resolve shocks or other discontinuities since they move with time. The best that can be done is a uniform grid of approximately square inviscid cells with boundary layer, wall-normal clustering.

VII. Example Test Cases

To test the capabilities of the new codes and validate the methods employed, two test cases have been analyzed from the prototype LENS-X facility. Both cases used a helium driver gas, air test gas, and air as an accelerant. Measured data for these two cases were the primary and secondary shock speed as measured by a series of time-of-arrival sensors, measured static wall pressure near the end of the acceleration tube and Pitot pressure probe measurements that were mounted on a rake across the acceleration tube near the static pressure location. The best-performing Pitot probe was selected for comparison. Although the Pitot probe was 5-cm from the centerline of the tube, the DPLR simulations for both runs showed that the radial gradients were negligible through most of the core of the tube. Hence, the exact location was extracted from the DPLR simulation for comparison, but the equivalent 1D value predicted by the *CHEETAh* and *Jaguar* simulations were simply compared directly.

A. LENS-X Run 5

The first run considered is Run 5 from the LENS-X series. The test pressures for the three sections of the facility were 8.3 MPa, 20.6 kPa, and 335 Pa. The driver temperature for this case was 428 K while the other two sections were at room temperature. The resulting freestream flow condition is at approximately 5 MJ/kg (3 km/s freestream velocity).

The comparisons with *CHEETAh* are considered first. The *CHEETAh* code was used to compute the flow conditions using four models: (1) equilibrium chemistry and thermodynamics, (2) equilibrium chemistry only with vibrational energy frozen at the initial state, (3) equilibrium thermodynamics with chemistry frozen at the initial state, and (4) perfect gas (no chemistry or vibration considered). For this relatively low enthalpy condition, there is some chemical dissociation but vibration is more dominant as an energy absorption mechanism. These four models are compared to the Pitot pressure trace in Fig 12(a) and to the static pressure trace in Fig 12(b). In all cases, the predicted test time is indicated by the horizontal extent of each line. As the lines show, the different thermochemical models result in significantly different characteristic wave angles. Two regions are shown with predicted levels and temporal duration for both the post-shock State 20 and the freestream State 5. The results show that both the Pitot and the static pressure values are captured between the thermochemical equilibrium and the perfect gas solutions. This makes sense because these two solutions represent the extremes that are possible. By treating either the vibration or the chemistry in equilibrium (but not both), the results fall midway between the two bounds. It was mentioned previously that at this energy level in the facility the gases are only mildly reacting and the bulk of the calorically-imperfect gas behavior is due to absorption of energy by vibrational excitation. This is clear from comparing to the solutions since the vibrational equilibrium and the full thermochemical equilibrium solutions closely match each other. The best match to the data in this case is the option with equilibrium chemistry but neglecting vibration. Perhaps this may be due to the fact that the vibrational mode relaxes slowly enough that the gas immediately downstream of each wave is close to frozen. Alternately it may simply be that the combined relaxation of all thermochemical modes coincidentally is approximately equal to the amount assumed by the equilibrium chemistry model. In any case, the perfect gas solution is the only one that is clearly incorrect because the test time durations are incorrect. The full thermochemical equilibrium model predicts reasonable test time and

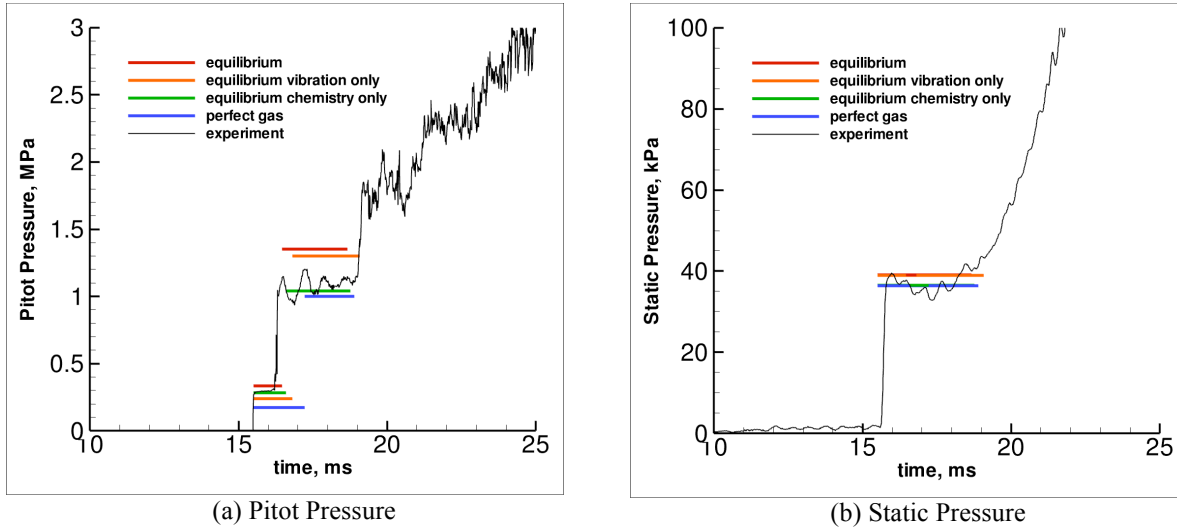


Figure 12. Comparison of Measured Run 5 Pitot and Static Pressure to *CHEETAh* Predictions with Various Thermochemical Model Options

static pressure values, although the freestream Pitot pressure is predicted slightly too high. As discussed during the outline of the algorithm, the *CHEETAh* code may optionally be anchored to a measured Pitot pressure for production runs.

Additionally, the *CHEETAh* code may be run in a mode where the primary and secondary shock speeds are specified as input rather than the driver and acceleration pressures. Normally, this would be done, but, in this case, the pressures were used to evaluate the capability of the code to predict the correct shock speed values. The comparisons are shown in Table 1. The measured values were quoted to be accurate to $\pm 5\%$, so, excepting one value, the predicted value by all models are well within the uncertainty bounds of the measure data. Since even the perfect gas case computes the correct shock speeds within the measurement uncertainty, these quantities are not sensitive enough to discern modeling differences from.

	Primary shock (km/s)		Secondary Shock (km/s)	
Measured	1.86	± 0.10	3.20	± 0.16
Equilibrium (full)	1.81	(-2.6%)	3.32	(+3.5%)
Equilibrium vibration	1.78	(-4.1%)	3.38	(+5.2%)
Equilibrium chemistry	1.85	(-0.8%)	3.22	(+0.6%)
Perfect gas	1.82	(-2.2%)	3.33	(+3.8%)

The full unsteady Navier-Stokes simulation with the DPLR code was also generated and the unsteady time history of the flow at the points where the Pitot probe and the static probe were located in the facility were extracted. Both air sections of the facility were modeled with 5-species non-equilibrium air chemistry and vibrational non-equilibrium. These comparisons are shown in Fig 13. Overall the DPLR agreement is similar to what has been observed with the other two codes. The Pitot pressure of the freestream gas is higher than the measured data, but the level obtained is almost exactly the same as the *CHEETAh* solution assuming equilibrium thermochemistry. This implies that the non-equilibrium component is not predicted by DPLR to be important for this particular flow. It also suggests that the simple characteristics based approach, which can be computed in a few seconds, can generate a result which has most of the essential physics of the full Navier-Stokes solution for the purpose of test condition and test data validation. The extent of test gas time as noted by the plateau of Pitot pressure between 16.5 ms and 21 ms is also predicted to be longer than the experiment suggests. This may possibly be a non-equilibrium effect since the test time is set by the propagation angle of the unsteady expansion waves and very small changes to the angle over the 25-m acceleration tube can dramatically change the arrival time of the waves. The discrepancy in test time prediction might also be caused by viscous effects too since doubts about the turbulence modeling for this type of flow have already been raised.

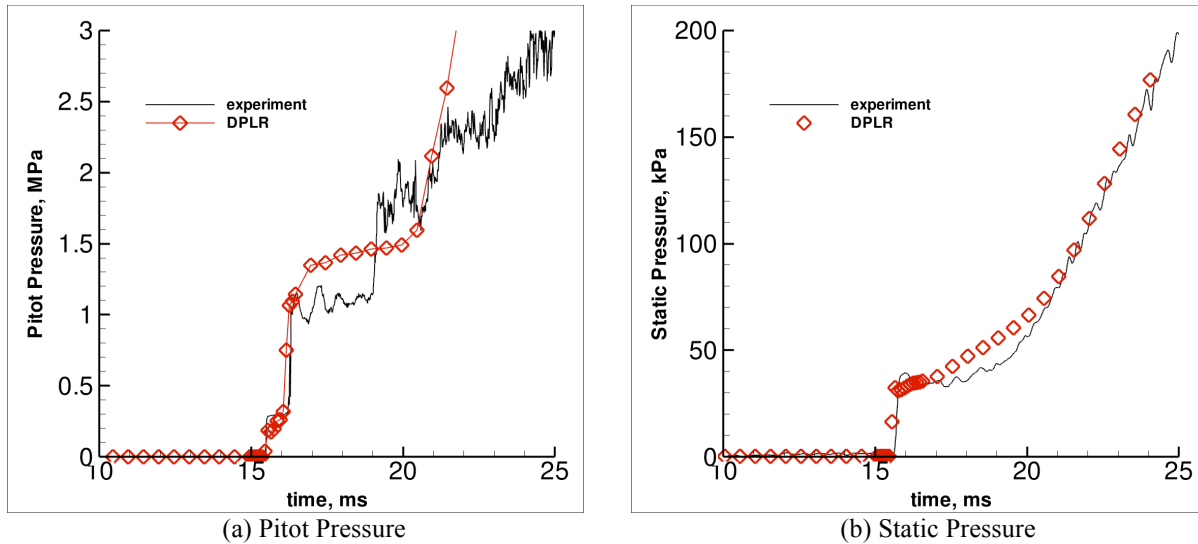


Figure 13. Comparison of Measured Run 5 Pitot and Static Pressure to *DPLR* Predictions

Finally, this case was simulated using the *Jaguar* one-dimensional Lagrangian code. The numerically generated wave diagram for this case is shown in Fig 14, which plots contours of density that were carefully selected to highlight the wave structure. Plotting uniform gradients of density is not useful to construct a picture such as this because the range of scale of densities in the different sections of the tunnel. A numerical wave diagram is useful to look at the interactions of the unsteady expansion in the secondary system to assess the possibility of the head of the wave reflecting off the contact surface to create non-linear interactions.

Similar to the set of solutions from the CHEETAH code, the *Jaguar* code has been used to generate four types of solutions. The first case is the perfect gas case. Second is non-equilibrium chemistry in the driven and acceleration sections, third is non-equilibrium vibration in the driven and acceleration sections but with no chemical dissociation, and fourth is with both chemical and vibrational non-equilibrium and vibration-dissociation coupling is handled with the Park $T-T_v$ model²⁷. The effect of chemistry on the problem is shown qualitatively in Fig 15, which plots the field of the most relevant excited species, nitric oxide and atomic oxygen. The zone of test gas at all times is bordered with a black line and the driver gas resides to the left of this outlined region and the acceleration gas resides to the right. As the chemistry contours show, there is significant nitric oxide and atomic oxygen in the accelerant gas once it is heated by the secondary shock, but neither of these species exists in significant quantities in the test gas downstream of the primary shock or through the unsteady expansion (approximately 0.4% NO and no O). For a 5 MJ/kg enthalpy condition in a reflected shock tunnel, approximately 5% nitric oxide by mass exists in the freestream. A slight amount of chemical non-equilibrium is evident immediately downstream of the secondary shock where some color variation exists in a very thin band, but the gas quickly goes to the equilibrium chemical state.

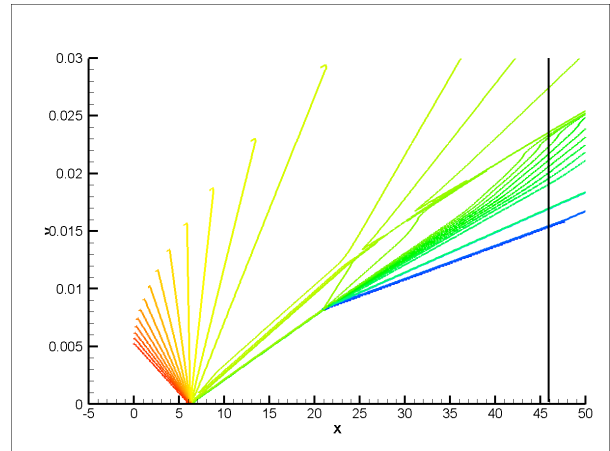


Figure 14. Numerical Wave Diagram Generated by *Jaguar* Code using Plot of Density Contours for LENS-X Run 5

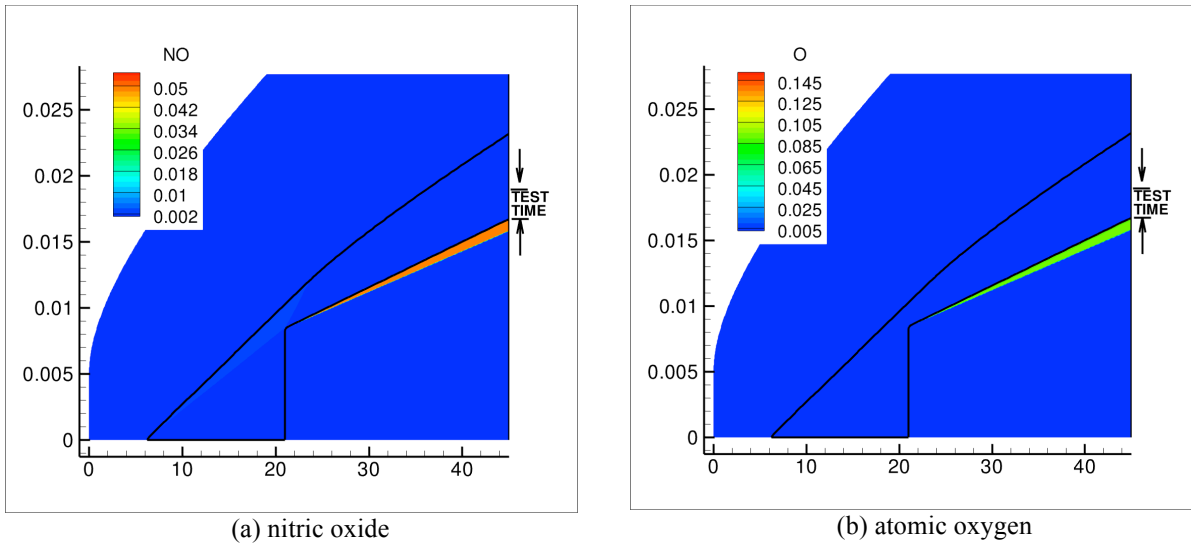


Figure 15. Predicted Excited Chemical Species for Run 5 using Jaguar Non-equilibrium Model

Finally, the comparison to the Pitot pressure and static pressure measurement is shown in the same way as for the other two codes in Fig 16. Here, the agreement is similar to what was obtained already with the DPLR and the *CHEETAh* simulations. Both the full non-equilibrium model and the model that considered non-equilibrium chemistry but ignored vibration accurately capture the state 20 Pitot pressure. The perfect gas and the frozen, non-equilibrium vibration model clearly predict the wrong contact surface speed as was observed with the Jaguar code. The state 5, freestream Pitot pressure is over-predicted consistently with the solution that the DPLR and the full equilibrium *CHEETAh* solutions gave. The state 5 test time predicted by all of the Jaguar models is shorter than observed in the experiment. At approximately 18ms, the Jaguar solutions experience a rise in Pitot pressure that seems to correspond roughly with the jump in level measured to indicate the start of the expansion waves. However, this jump is predicted to occur too early relative to what was observed in the measurements. All of the Jaguar simulations were cut off at the arrival of the driver gas at the Pitot probe location just because of a minor post-processing issue with regard to extracting Pitot pressure from the unsteady data. This has nothing to do with the solver itself. Finally, the static pressure comparison is also given in Fig 16(b). As we have observed previously in the comparisons with *CHEETAh* and DPLR, the static pressure is predicted better than the Pitot pressure seems to be by all the models.

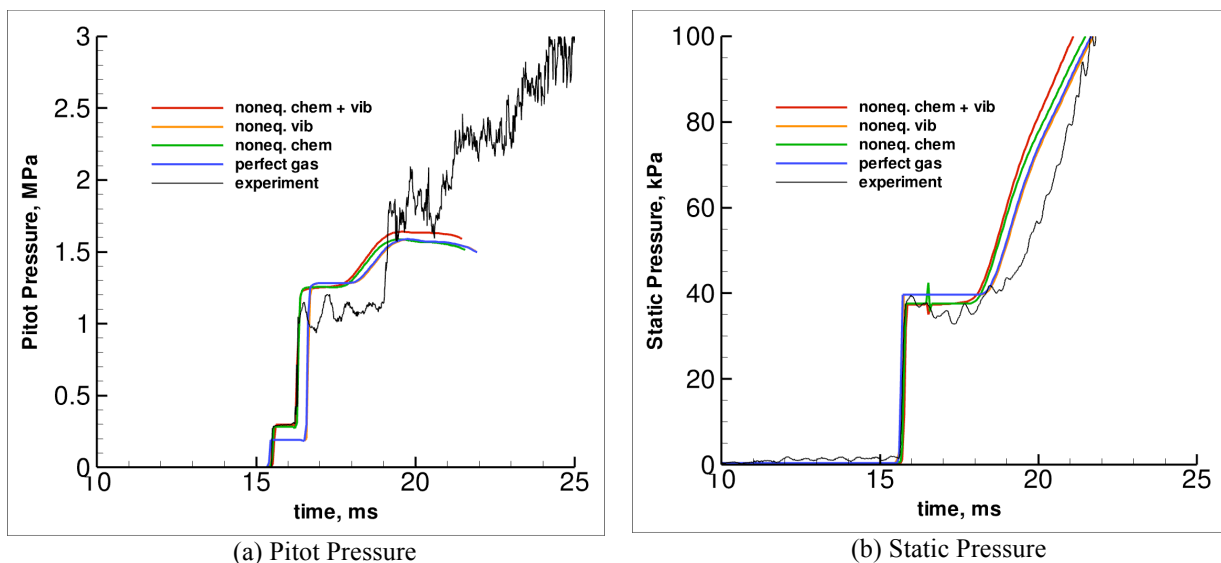


Figure 16. Comparison of Measured Run 5 Pitot and Static Pressure to Jaguar Predictions

B. LENS-X Run 6

The first run considered is Run 5 from the LENS-X series. The test pressures for the three sections of the facility were 13.8 MPa, 10.1 kPa, and 40 Pa. The driver temperature for this case was 350 K while the other two sections were at room temperature. The resulting freestream flow condition is at approximately 8.5 MJ/kg (4 km/s freestream velocity).

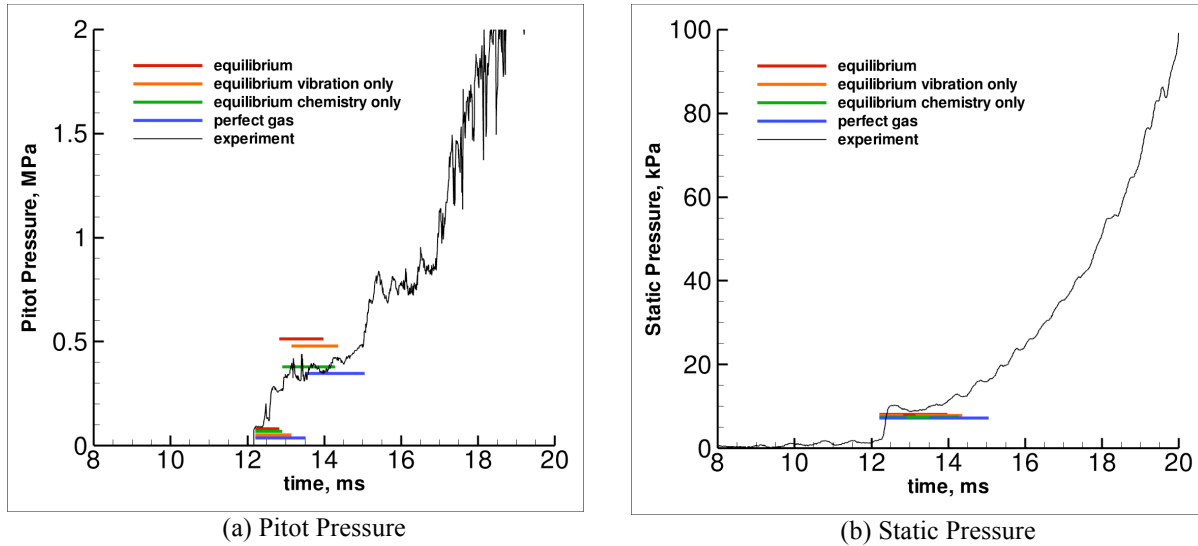


Figure 17. Comparison of Measured Run 6 Pitot and Static Pressure to *CHEETAh* Predictions with Various Thermochemical Model Options

The comparisons between the *CHEETAh* code and the measured data are given in Fig 17(a) for the Pitot pressure and in Fig 17(b) for the static wall pressure. Here, the trends in the comparisons are similar to those observed for Run 5. The Pitot pressure State 20 level and State 5 freestream level observed in the experimental measurements are again bounded between the perfect gas prediction and the equilibrium thermochemistry prediction. We observe that again for Run 6, the model assuming equilibrium chemistry and frozen vibrational energy seems to agree best with the measurements.

We cannot conclude that this is a general result yet until many more measurements are made available, but it is encouraging to see that the numerical tool seems to be consistent. As before, the full equilibrium thermochemistry case predicts test times and notional levels reasonably well, although the freestream Pitot pressure is over-predicted by approximately the same percentage as in Run 5. Further, the perfect gas option again produces test times that are clearly incorrect compared to the measurements. Finally, the comparisons with the measured shock velocities are shown in Table 2. With the 5% measurement uncertainty, both primary and secondary shock speeds are again predicted with one exception. We observe once more that accurately predicting the shock velocities will be required for accurate freestream prediction, but successfully predicting these quantities is not a guarantee of accurate modeling the freestream thermodynamic state.

	Primary shock (km/s)		Secondary Shock (km/s)	
Measured	2.13	±0.11	4.33	±0.22
Equilibrium (full)	2.09	(-1.9%)	4.31	(-0.5%)
Equilibrium vibration	2.02	(-5.2%)	4.36	(+0.7%)
Equilibrium chemistry	2.13	(+0.0%)	4.17	(-3.8%)
Perfect gas	2.08	(-2.3%)	4.29	(-0.9%)

The predictions from the unsteady Navier-Stokes simulation with the DPLR code are shown in Fig 18. The comparison with the Pitot pressure shown in Fig 18(a) revealed an interesting behavior. The State 20 Pitot pressure level (the point at 12.25-ms) is accurately predicted by the DPLR simulation. However, while the CHEETAH solution Fig 17(a) predicted the next plateau of Pitot pressure from the 13-ms to 15-ms range, the DPLR simulation shows this level only very briefly before rising to the third plateau in the measure data. Although the duration of this new level is not very accurately predicted, DPLR does accurately predict the wave structure that causes the change in the state. If the DPLR simulation data is extracted at a time of 13-ms, the individual freestream properties agree very well with the predicted CHEETAH properties. Both codes predict the freestream velocity to be about 3.8 km/s with a total enthalpy of 8.3-8.4 MJ/kg. Density is predicted to be 0.030 kg/m³ and 0.028 kg/m³ respectively. The static pressure predicted by DPLR also agrees quite well with the data as shown in Fig 18(b).

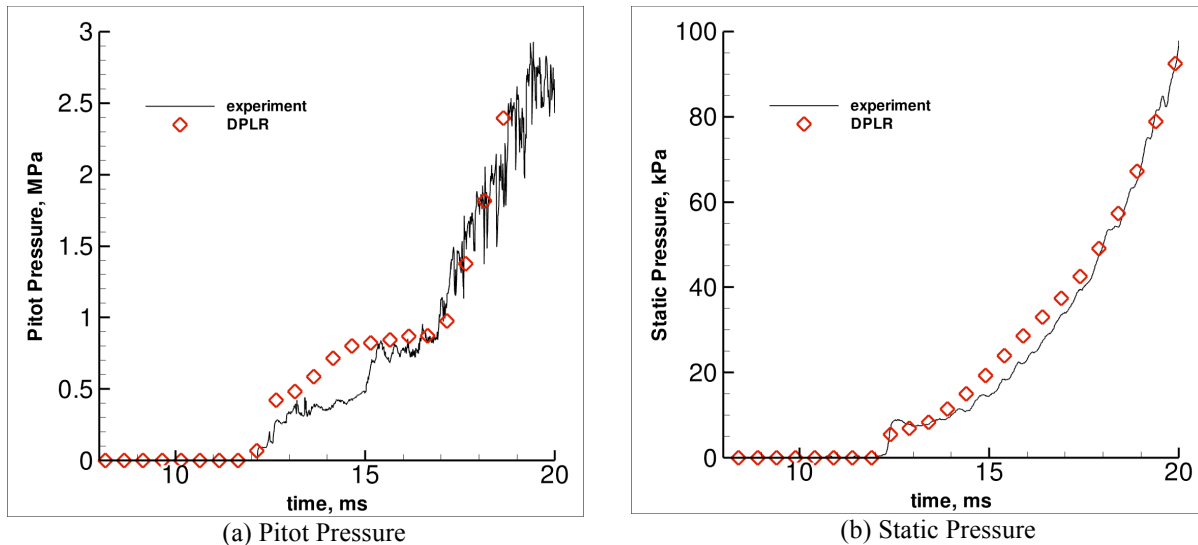


Figure 18. Comparison of Measured Run 6 Pitot and Static Pressure to *DPLR* Predictions

If the properties are extracted from DPLR at a time of 16ms, the state of the flow has changed to a velocity of 3.2 km/s, total enthalpy of 6.0 MJ/kg, and static density of 0.091 kg/m³. The reason for this prediction is unclear, though a study of the large volume of unsteady data seems to suggest that it is, in some way, caused by the propagation of waves through the test gas cause by thermal gradients, which translate into different speeds of sound. Obviously this does not occur in the experiment in the same way, but DPLR seems to predict the state of the next plateau of Pitot pressure observed from 15.5ms to 17ms at the end of the freestream test flow. Further study needs to be done with this simulation to see whether useful information about expansion tunnel operation can be extracted to better predict such phenomena.

Finally, the wave diagram computed with the Jaguar code is shown in Fig 19. Again, the selection of density contours to highlight the wave structure must be carefully done, but the states are evident in the diagram when comparing to the analytical Fig 2. For this case, the chemical dissociation was analyzed as it was for run 5 by plotting nitric oxide and atomic oxygen contours in the zones of the domain as shown in Fig 20. The test gas zone is outlined in black with the driver zone to its left and the acceleration gas to its right. Here, the level of atomic oxygen is observed to be negligible in the test gas as it was for run 5. The oxygen in the acceleration gas behind the secondary shock is totally dissociated but no atoms are formed in the test gas downstream of the primary shock because of the low pressure. For nitric oxide, however, a small amount of formation occurs in the test gas zone. This constituent peaks at a value of approximately 1% by mass, which may still be considered very small relative to

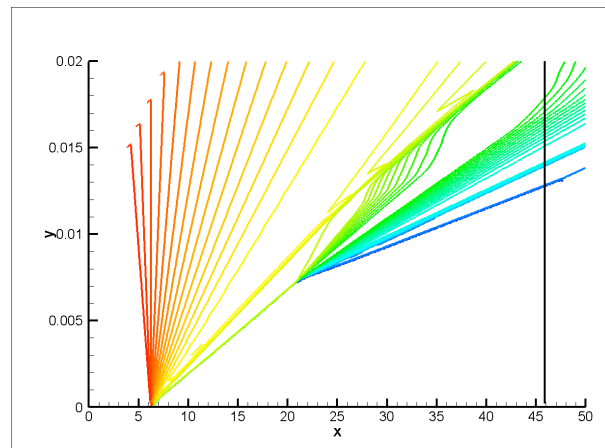


Figure 19. Numerical Wave Diagram Generated by Jaguar Code using Plot of Density Contours for LENS-X Run 6 (perfect gas model)

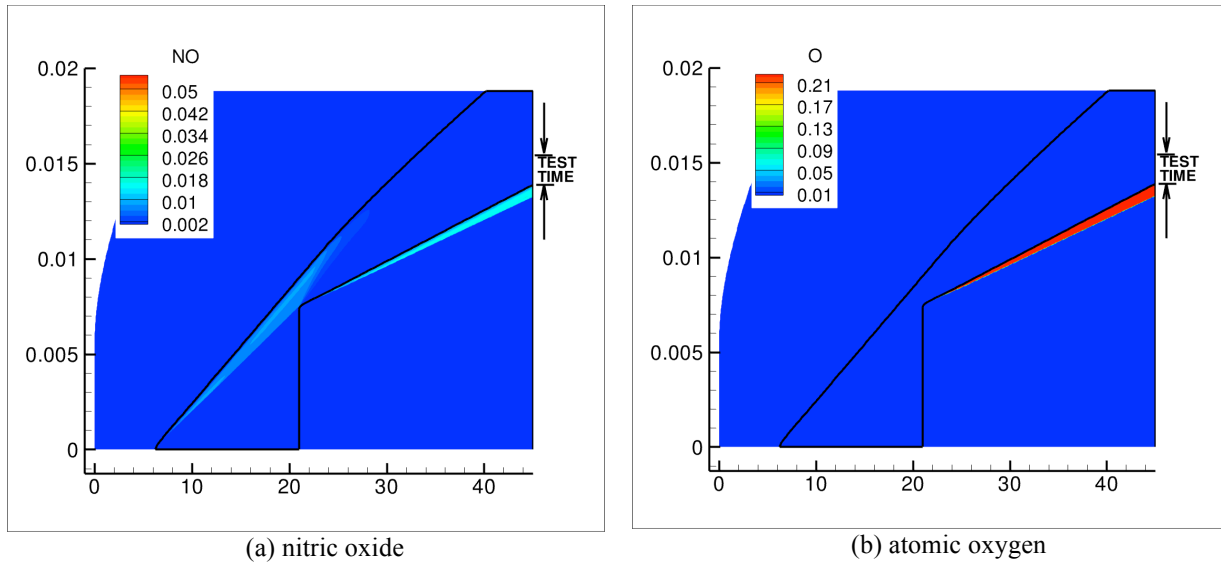


Figure 20. Predicted Excited Chemical Species for Run 6 using Jaguar Non-equilibrium Model

a reflected shock tunnel. However, the unsteady expansion cools the test gas off and the nitric oxide is completely eliminated in the freestream zone of the facility. It is also worth noting that the level of nitric oxide in the acceleration section downstream of the secondary shock is only at approximately 2% by mass. This is because the temperature in the acceleration gas is high enough (about 4,500K) that nitric oxide formation is no longer a preferred dissociation mechanism. At higher energy levels, the acceleration gas will ionize, a feature that is also built into all three code tools.

Finally, the Pitot pressure comparison to the Jaguar solution is shown in Fig 21(a) and the static pressure comparison is shown in Fig 21(b), where the static pressure is once more well-predicted by all models. Again, we observe that the full non-equilibrium model and the model with non-equilibrium chemistry best match the state 20 Pitot measurement and duration. As with the DPLR simulation, the predicted state 5 Pitot pressure quickly rises past the plateau of Pitot pressure defining the freestream state and reaches a level consistent with the third plateau of Pitot pressure between 15.5ms and 17ms. As with the DPLR simulation, the reasons for this behavior are not yet clear, but the use of the Jaguar code provides an alternative mechanism to explore the behavior using simulations that take only one or two minutes to perform.

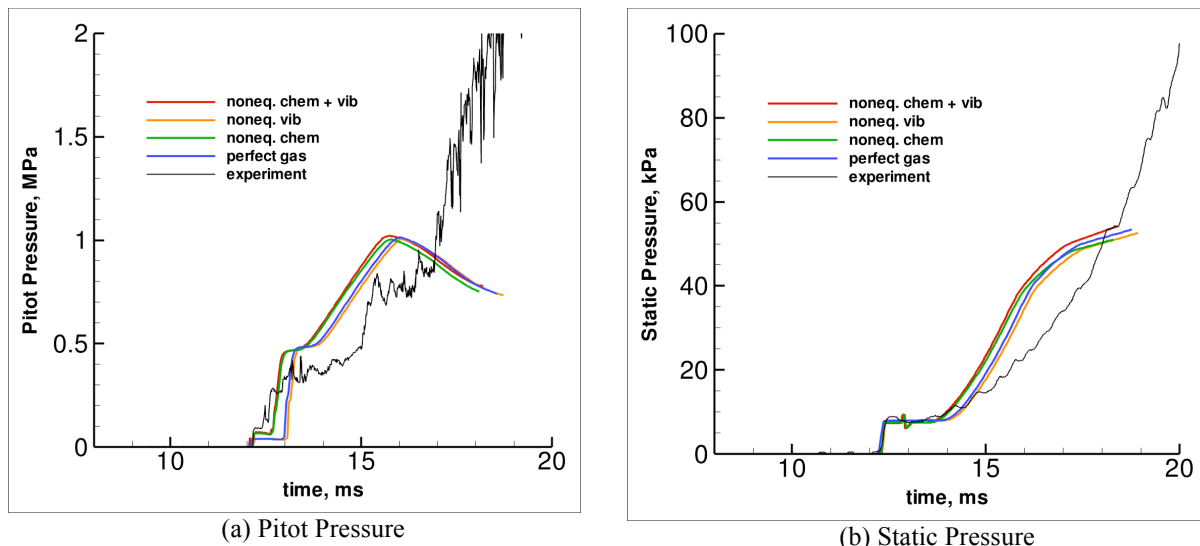


Figure 21. Comparison of Measured Run 6 Pitot and Static Pressure to Jaguar Predictions

VIII. Conclusions

The computation of the conditions in the LENS-XX expansion tunnel facility has been demonstrated by employing three unique methods of solution. These techniques have been built upon existing methodologies and extended and modified to incorporate physics specific to the LENS-XX expansion tunnel facility operation. The first technique employed is a characteristics based approach where the exact jumps across the primary and secondary waves systems are computed for arbitrary gas mixtures and thermodynamics states. The second technique employed is an unsteady Lagrangian shocktube algorithm that has been extended to include vibrational and chemical non-equilibrium. The third technique employed is the simulation of full unsteady, viscous problem using a robust, proven Navier-Stokes solver.

Several critical physical phenomena have been outlined that were considered in the building of these codes. First, the modeling of expanding hydrogen has been considered with regard to the unusual rotational excitation of diatomic hydrogen molecules that results in the rotational specific heat of the gas being treated differently than the standard, fully-excited diatomic gas. Next, the effects of non-ideal equation of state have been considered by employing a modified equation of state for the very dense gases that exist in the driver chamber of the facility. Finally, the consideration of chemical dissociation and thermodynamic excitation has been considered through equilibrium and non-equilibrium models that deviate from the calorically perfect gas approximation that is often made for expansion tunnel facility operation.

These three methods have been compared to two cases from the LENS-X prototype facility as validation for use in the newly operational LENS-XX expansion tunnel facility. Several lessons were learned from these comparisons. First, the consideration of chemical and thermodynamic excitation is critical for even low enthalpy conditions. The most consistent result obtained by comparing the results of each code algorithm to the experimental data was that the test times predicted by the perfect gas model were clearly incorrect. This error is caused by incorrect wave propagation rates stemming from errors in the perfect gas sound speed. Over the length of a facility on the scale of LENS-XX, even a small error in wave speed results in significant discrepancies from the observed behavior.

We have observed that, for the two cases studied, the characteristics based CHEETAh code is capable of reproducing the measured behavior of the facility when the correct thermochemical models are selected. Many more test cases need to be considered to fully validate this tool, but the initial results suggest that this tool may be adequate for a production freestream condition test code. The unsteady one-dimensional and two-dimensional simulations suggest the interaction of waves occurring in the predicted test gas that in some ways deviate from the measured behavior of the test gas, but in other ways tantalizingly suggest that some of the basic phenomena relevant to the operation of the facility may be captured numerically. Additional work with both of them needs to be performed to fully understand their place in the analysis of the facility.

We must emphasize that this effort is a first step in characterizing the operation of a large-scale expansion tunnel facility with the goal of turning LENS-XX into a turnkey, production wind tunnel facility for high enthalpy reentry applications. This goal can only be achieved through repeated validation of the facility and its test articles with supporting CFD as we have done with the LENS-I and LENS-II reflected shock tunnel facilities. However, this initial step has demonstrated some encouraging results that have validated the basic approaches taken and further work both experimentally and computationally will be performed in parallel in the near future.

References

- ¹Holden, M.S. and Parker, R.P. "LENS Hypervelocity Tunnels and Application to Vehicle Testing at Duplicated Flight Conditions," Chp 4 of *Advanced Hypersonic Test Facilities*. Lu, F.K. and Marren, D.E. Eds. AIAA Progress in Astronautics and Aeronautics Series: Vol 198. Chapter 4. Reston, VA: American Institute of Aeronautics and Astronautics, 2002.
- ²Holden, M.S.; Wadhams, T.P.; and Candler, G.V. "Experimental Studies in the LENS Shock Tunnel and Expansion Tunnel to Examine Real-Gas Effects in Hypervelocity Flows". AIAA Paper 2004-0916. January 2004.
- ³Parker, R.; Wakeman, T.; Holden, M.; and MacLean, M. "Measuring NO Freestream Concentration Using Quantum Cascade Lasers at CUBRC". AIAA Paper 2006-0926. 44TH Aerospace Sciences Meeting & Exhibit. Reno, NV: 9-12 January 2006.
- ⁴MacLean, M.; Candler, G.; and Holden, M. "Numerical Evaluation of Flow Conditions in the LENS Reflected Shock-Tunnel Facilities". AIAA Paper 2005-0903. 43RD Aerospace Sciences Meeting & Exhibit. Reno, NV: 10-13 January 2005.
- ⁵Dufrene, A.; Sharma, M.; and Austin, J.M. "Design and Characterization of a Hypervelocity Expansion Tube Facility," AIAA Paper 2007-1327. 45TH Aerospace Sciences Meeting & Exhibit. Reno, NV: 8-11 January 2007.
- ⁶Nompelis, I.; Candler, G.; Wadhams, T.; and Holden, M. "Numerical Simulation of the High-Enthalpy Experiments in the LENS-X Expansion Tube Facility," AIAA Paper 2004-1000. 42ND Aerospace Sciences Meeting & Exhibit. Reno, NV: 5-8 January 2004.
- ⁷Erds, J.; Bakos, R.; Castrogiovanni, A.; and Roders, C. "Dual Mode Shock-Expansion/Reflected-Shock Tunnel," AIAA Paper 97-0560. 35TH Aerospace Sciences Meeting & Exhibit. Reno, NV: 3-6 January 1997.

- ⁸Miller, C.G., III. "A Program for Calculating Expansion-Tube Flow Quantities for Real-Gas Mixtures and Comparison with Experimental Results," NASA TN-D-6830. Langley Research Center: 1 September, 1972.
- ⁹Trimpi, R.L. "A Preliminary Theoretical Study of the Expansion Tube, A New Device for Producing High-Enthalpy Short-Duration Hypersonic Gas Flows," NASA TR R-133. Langley Research Center: 1 January, 1962.
- ¹⁰Gordon, S. and McBride, B. "Computer Program for Calculation of Complex Chemical Equilibrium Compositions and Applications," NASA RP-1311. October 1994.
- ¹¹Sharma, S. and Park, C. "Operating Characteristics of a 60- and 10-cm Electric Arc-Driven Shock Tube – Part I: The Driver," *Journal of Thermophysics and Heat Transfer*, Vol 4, no 3. Pgs 259 – 265. July 1990.
- ¹²Jacobs, P.A.; Silvester, T.B.; Morgan, R.G.; Scott, M.P.; Gollan, R.J.; and McIntyre, T.J. "Superorbital Expansion Tube Operation: Estimates of Flow Conditions via Numerical Simulation," AIAA Paper 2005-0694. 43RD Aerospace Sciences Meeting & Exhibit. Reno, NV: 10-13 January 2005.
- ¹³P. A. Jacobs. "Shock tube modeling with L1d". Department of Mechanical Engineering Report 13/98, The University of Queensland, Brisbane, Australia., November 1998.
- ¹⁴Candler, Graham V. "Hypersonic Nozzle Analysis Using an Excluded Volume Equation of State". AIAA Paper 2005 – 5202. 38TH AIAA Thermophysics Conference, Toronto, CA: 6 – 9 June 2005.
- ¹⁵Lordi, J.A. and Mates, R.E. "Non-equilibrium Expansions of High-Enthalpy Airflows." Cornell Aeronautical Laboratory Report, ARL 64-206. November 1964.
- ¹⁶Svehla, R. "Estimated Viscosities and Thermal Conductivities of Gases at High Temperatures," NASA TR R-132. 1962 .
- ¹⁷Irwin, Patrick. *Giant Planets of Our Solar System*. Chichester, UK: Springer-Praxis. 2003.
- ¹⁸Jacobs, P.A. "Approximate Riemann Solver for Hypervelocity Flows," AIAA Journal, Vol 30, no 10. Pgs 2558 – 2561. October 1992.
- ¹⁹McBride, B.; Zehe, M.; and Gordon, S. "NASA Glenn Coefficients for Calculating Thermodynamic Properties of Individual Species," NASA TP-2002-211556. September 2002.
- ²⁰Wright, M.J.; Bose, D.; and Candler, G.V. "A Data Parallel Line Relaxation Method for the Navier-Stokes Equations". *AIAA Journal*. Vol 36, no 9. Pgs 1603 – 1609. Sept 1998.
- ²¹MacCormack, R.W. and Candler, G.V. "The Solution of the Navier-Stokes Equations Using Gauss-Seidel Line Relaxation". *Computers and Fluids*. Vol 17, No 1. Pgs 135 – 150. 1989.
- ²²Candler, G.V. "Chemistry of External Flows". *Aerothermochemistry for Hypersonic Technology*: Von Karman Institute for Fluid Dynamics Lecture Series. VKI LS 1995-04.
- ²³Landau, L. and Teller, E. "Theory of Sound Dispersion". *Physikalische Zeitschrift der Sowjetunion*. Vol 10, no 34. 1936.
- ²⁴Millikan, R. and White, D. "Systematics of Vibrational Relaxation". *Journal of Chemical Physics*. Vol 39, no 12. Pgs 3209 – 3213. 1963.
- ²⁵Camac, M. "CO₂ Relaxation Processes in Shock Waves". *Fundamental Phenomena in Hypersonic Flow*. J.G. Hall Ed. Cornell University Press. Pgs 195 – 215, 1964.
- ²⁶Park, C.; Howe, J.T.; Jaffe, R.J.; and Candler, G.V. "Review of Chemical-Kinetic Problems of Future NASA Missions II: Mars Entries". *Journal of Thermophysics and Heat Transfer*. Vol 8, no 1. Pgs 9 – 23. 1994.
- ²⁷Park, Chul. "Assessment of Two-temperature Kinetic Model for Ionizing Air". AIAA Paper 87-1574. AIAA 22ND Thermophysics Conference. Honolulu, HI: 8-10 June 1987.
- ²⁸Marrone, P.V. and Treanor, C.E. "Chemical Relaxation with Preferential Dissociation from Excited Vibrational Levels". *The Physics of Fluids*, Vol 6, no 9. Pgs 1215 – 1221. September 1963.
- ²⁹Palmer, G.E. and Wright, M.J. "A Comparison of Methods to Compute High Temperature Gas Viscosity". *Journal of Thermophysics and Heat Transfer*. Vol 17, no 2. Pgs 232 – 239. 2003.
- ³⁰Palmer, G.E. and Wright, M.J. "A Comparison of Methods to Compute High Temperature Gas Thermal Conductivity". AIAA Paper 2003-3913. Jun 2003.
- ³¹Gupta, R.; Yos, J.; Thompson, R.; and Lee, K. "A Review of Reaction Rates and Thermodynamic and Transport Properties for an 11-Species Air Model for Chemical and Thermal Nonequilibrium Calculations to 30000 K". NASA RP-1232. August 1990.
- ³²Ramshaw, J.D. "Self-consistent Effective Binary Diffusion in Multicomponent Gas Mixtures". *Journal of Non-Equilibrium Thermodynamics*. Vol 15, no 3. Pgs 295 – 300. 1990.
- ³³Baldwin, B.S. and Lomax, H. "Thin Layer Approximation and Algebraic Model for Separated Turbulent Flows". AIAA Paper 78-0257. Huntsville, AL: 1978.
- ³⁴Spalart, P.R. and Allmaras S.R. "A One-Equation Turbulence Model for Aerodynamic Flows". AIAA Paper 92-0439. 30TH Aerospace Sciences Meeting & Exhibit. Reno, NV: 6-9 Jan, 1992.
- ³⁵Menter, F.R. "Two-Equation Eddy-Viscosity Turbulence Models for Engineering Applications". *AIAA Journal*. Vol 32, no 8. Pgs 1598 – 1605. August 1994.
- ³⁶Brown, James. "Turbulence Model Validation for Hypersonic Flow". AIAA Paper 2002-3308. 8TH Thermophysics and Heat Transfer Conference. St. Paul, MN: 24 – 26 Jun 2002.
- ³⁷Catris S. and Aupoix B. "Improved Turbulence Models for Compressible Boundary Layers." AIAA Paper 98-2696. 2ND Theoretical Fluid Mechanics Meeting: Albuquerque, NM, June 1998.
- ³⁸Rumsey, C.L.; Sanetrik, M.D.; Biedron, R.T.; Melson, N.D.; and Parlette, E.B. "Efficiency and Accuracy of Time-Accurate Turbulent Navier-Stokes Computations," *Computers & Fluids*, Vol 25, No 2. Pgs 217 – 236. 1996.